Estimation and Evaluation of the FY-3D/MERSI-II Fractional Snow Cover in China

Jinyu Huang, *Student, IEEE*, Lingmei Jiang, *Member, IEEE*, Fangbo Pan, Bo Zhong, Shengli Wu, *and* Huizhen Cui

***Abstract*—The frequent occurrence of intense snowfall events and extreme temperature fluctuations in China significantly hampers the precise monitoring of snow-covered areas. The provision of near-real-time monitoring of fractional snow cover in China is essential to bolster disaster management initiatives. The Medium Resolution Spectral Imager (MERSI-II), aboard the FengYun-3D satellite, presents significant capabilities for effective snow monitoring. The aim of this study was to enhance the multiple endmember spectral mixture algorithm based on automatic extraction of endmembers (MESMA-AGE) for estimating FY-3D/MERSI-II fractional snow cover (FSC) in China. The accuracy of these estimations was corroborated using 30-m FSC maps derived from Landsat-8/OLI images. This validation process resulted in RMSE and R^2 values of 0.13 and 0.88, respectively, across 253 OLI-based FSC scenes. The study examined and analyzed the effects of diverse land cover types and complex terrain on the FSC estimates, focusing specifically on three major snow-covered areas in China. In comparison to areas with cultivated land and sparse vegetation, bare surfaces yielded the most accurate results, whereas forest regions showed the lowest accuracy. The comparative analysis revealed that the Tibetan Plateau and Northern Xinjiang achieved high accuracy in mapping snow cover. The maps of Northeast China were less precise, largely due to the prevalence of forests. Additionally, while the MERSI-II FSC is effective in monitoring snow cover on flat plains, its performance is less reliable in steep terrain. Moreover, the comparison between MERSI-II and MODIS FSC indicated that MERSI-II has a marked advantage in areas with substantial snow cover.**

***Index Terms*—fractional snow cover area, FY-3D, spectral mixture analysis, validation**

I. INTRODUCTION

As a notable reflector of solar radiation, snow significantly influences the surface radiation and energy balance due to its high albedo and low thermal diffusivity [1-4]. Moreover, the broad distribution of snow across China in winter leads to profound negative impacts of severe snowfall events on domestic agriculture, the economy, and society [5]. This situation underscores the critical necessity for large-scale, high-frequency monitoring of snow cover in China, which is vital for effective disaster management and response strategies.

In recent years, numerous snow mapping algorithms have been developed to retrieve fractional snow cover areas. Multivariate polynomial regression approaches have been established for estimating fractional snow cover (FSC) using indicators such as the normalized difference snow index (NDSI) [6, 7], the universal ratio snow index (URSI) [8], and the normalized difference forest snow index (NDFSI) [9]. The method of estimating snow area by relying only on the linear statistical relationship formed by the snow index in a local area has been proven to have limitations under various conditions. These limitations, verified by physical models [10], include factors like fluctuating snow grain sizes, the presence of impurities, and blockages resulting from forest canopies. Additionally, the use of machine learning algorithms for snow-covered area estimation is an emerging trend [11-14]. However, these studies often deal in developing "locally adaptive" machine learning algorithms for monitoring snow cover areas, rather than exploring their implementation for globally-scaled FSC estimation. Spectral mixing analysis (SMA) algorithms, rooted in physical theory, have gained increasing attention for monitoring snow-covered areas [15-19]. The linear mixture modelling technique was initially applied to estimate fractional snow cover areas via the use of a unique set of endmembers [17, 20]. Accounting for different spectral distributions of the same geographical object [21]—attributable to varying grain sizes, atmospheric, terrain, and surrounding object conditions—multiple endmember spectral mixture analysis (MESMA) model approaches are more suitable for retrieving snow cover areas [15, 16, 22-25]. MODIS Snow-Covered Area and Grain size (MODSCAG) products involve the use of model calculations and hyperspectral reflectance measurements to simulate the varying spectra of snow endmembers [15]. To enhance the universality and automation degree of the MESMA algorithm on a large spatial scale, a variant known as the MESMA algorithm based on automatic extraction of endmembers (MESMA-AGE) have evolved greatly [16, 22]. Over the years, the sophistication and robustness of the MESMA-AGE algorithm have improved. This refined technique is now extensively employed across an array of moderate- to high-spatial-resolution optical remote sensing

This work was supported in part by the National Key Research and Development Program of China under Grant 2022YFF0801302 and in part by the National Natural Science Foundation of China under Grant 42171317(Corresponding author: Lingmei Jiang).

Jinyu Huang, Lingmei Jiang, and Fangbo Pan are with the State Key Laboratory of Remote Sensing Science, jointly sponsored by Beijing Normal University and the Aerospace Information Research Institute of the Chinese Academy of Sciences, Faculty of Geographical Science, Beijing Normal University, Beijing 100875, China (e-mail: huangjy@mail.bnu.edu.cn; jiang@bnu.edu.cn; panfb@mail.bnu.edu.cn).

Bo Zhong is with the Aerospace Information Research Institute, Chinese Academy of Sciences, Beijing 100101, China (e-mail: zhongbo@radi.ac.cn)

Shengli Wu is with the National Satellite Meteorology Center, Beijing 100081, China (e-mail: wusl@cma.gov.cn)

Huizhen Cui is with the National Space Science Center, Chinese Academy of Sciences, Beijing 100190, China (e-mail: cuihuizhen@nssc.ac.cn)

platforms, encompassing Landsat-8/Operational Land Imager (OLI), Moderate-Resolution Imaging Spectroradiometer (MODIS), and Advanced Very High Resolution Radiometer (AVHRR)-2/3 [15, 16, 22, 23, 25].

The current capabilities of FY-3D/MERSI-II snow cover products fall short in meeting the temporal frequency and spatial resolution prerequisites vital for effective disaster early warning systems. FY-3 Multi-Sensor Synergy (MULSS) Snow Cover products, provided by the National Satellite Meteorological Center (NSMC), are derived from the Medium Resolution Spectral Imager-I (MERSI-I) and Visible and Infra-Red Radiometer (VIRR) sensors on FY series satellites. These products categorize pixels into two groups, i.e., snow and snow-free pixels, by employing a threshold method akin to the SNOMAP algorithm [26]. Given the inherent systematic discrepancies introduced when applying the above classification algorithms to coarser-resolution imagery, the resultant precision of these products is compromised.

The Chinese snow cover products are insufficient to support disaster monitoring and early warning in terms of both the temporal frequency and spatial resolution. The purpose of this study was to fully leverage the high-frequency and wide-observational capabilities of the FY-3D satellite, applying the MESMA-AGE algorithm to estimate FSC in China. We employ the Level-2A surface reflectance data products provided by [27] as the research data. Then, the results were evaluated via a comparison with Landsat-8/OLI snow cover maps. The disparities between the MERSI-II FSC (Fractional Snow Cover) and MODIS FSC data were quantitatively analyzed to evaluate the potential of Chinese optical sensors in the realm of snow cover monitoring.

The remainder of this paper is organized as follows: in Section II, an overview of the study region and materials is provided. Section III describes snow cover mapping methodologies. Section IV details the validation and comparison metrics employed to assess the performance of the MESMA-AGE algorithm. In Sections V and VI, a summary and conclusions are presented, respectively.

II. Study Region and Materials

A. *Study Region*

The performance of the FY-3D MERSI-II fractional snow cover mapping was evaluated over all snow-covered areas in China. It has been previously shown that China has an average annual snow area of approximately 9 million km^2 [28]. Therefore, three relatively stable snow-covered regions in China were selected to evaluate the snow cover map derived from FY-3D/MERSI-II images of China. These three stable snow-covered areas can be seen in Fig. 1, including Northeast China (A), the Tibetan Plateau (B), and northern Xinjiang (C). The Tibetan Plateau experiences low temperatures, minimal precipitation, and high wind speeds in winter owing to its high altitude [29]. This leads to a widespread, patchy distribution of thin, quickly melting snow over the internal plateau [30]. Further, the Tibetan Plateau is influenced by multiple climatic systems, including the Indian Monsoon in summer, the mid-latitude Westerlies in winter and the East Asian Monsoon in the east [31, 32]. In winter, the abundant water vapor is blocked by the southern and western boundaries of the Plateau, and gives rise to more precipitation over mountains. This sharply differs from the snow distribution in Northeast China, which (from northwest to southeast) contains the Greater Khingan range, Northeast China Plain, and Paektu Mountain. The fractional forest cover in these regions is approximately 0.4 [33, 34], significantly enhancing the snow storage capacity in this area. Here, snow typically falls from the end of November to mid-March, resulting in a fairly homogenous snow cover [9]. Compared to this area, northern Xinjiang exhibits a snow cover duration (SCD) of approximately 170 days, with the annual cumulative snow depth reaching 5.8 m [35]. Spring floods, caused by snowmelt, are important for agricultural irrigation in this region.

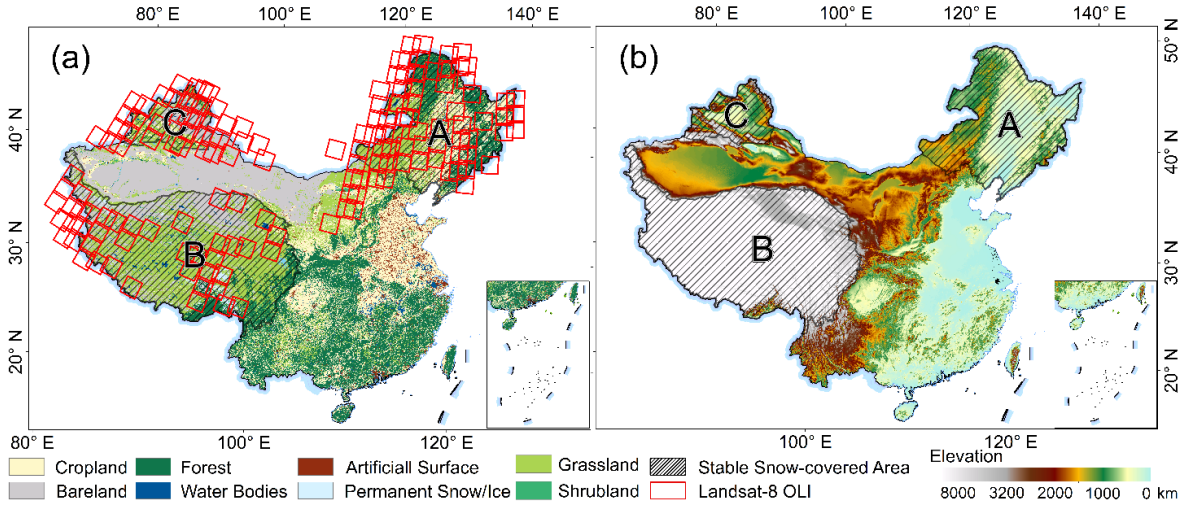

Fig. 1. Land cover map along with the locations of Landsat-8 OLI image areas (a) and elevations (b) in China. Land cover type is obtained from Globeland30 data set (https://www.webmap.cn/mapDataAction.do?method=globalLandCover). The terrain condition is represented by SRTM (https://srtm.csi.cgiar.org). A. Northeast China. B. The Tibetan Plateau. C. The Northern Xinjiang.

B. *MERSI surface reflectance data*

FY-3D is the 4th flight unit of the FY-3 satellite series, which was launched at the end of 2017. It can implement all-weather, multispectral, and three-dimensional observations of the global atmosphere and geophysical objects [36]. MERSI-II, designed to combine the function of the Medium Resolution Spectral Imager-I (MERSI-I) and Visible and Infrared Red Radiometer (VIRR), is equipped with a total of 25 channels and two spatial resolutions of 250 and 1000 m. Compared with the single-width spectral window bands of MERSI-I, the infrared detection capability of MERSI-II is substantially enhanced [37]. Furthermore, it has been demonstrated that the calibration accuracy and sensitivity of MERSI-II surpass those of the previous generation [38]. The MERSI-II sensor is notable for its high temporal frequency, broad field of view, and superior hyperspectral imaging capabilities. These qualities render it an exceptional tool for near-real-time retrieval of fractional snow cover areas across China.

The MERSI-II-based surface reflectance data have been preprocessed via radiometric calibration, atmospheric correction [27], and geometric registration and projected to the MODIS sinusoidal grid of 460 nonoverlapping tiles that measure approximately 10°×10°. TABLE I presents the spectral channel of the FY-3D/MERSI-II surface reflectance products alongside those of the MOD09GA products. In this study, we developed a snow cover mapping algorithm utilizing the reflectance in six bands, namely, bands 1 (0.470 μm), 2 (0.550 μm), 3 (0.650 μm), 4 (0.865 μm), 6 (1.640 μm), and 7 (2.130 μm). As shown in Fig. 2, we compared the different spectral channels of the MERSI-II and MODIS sensors. The pixels used for comparison were randomly sampled from MODIS and MERSI-II images. All the results demonstrated that the surface reflectance values of MERSI-II and MODIS in the different bands are consistent.

TABLE I
SPECTRAL CHANNELS OF FY-3D/MERSI-II SURFACE PRODUCTS AND MOD09GA PRODUCTS

	FY-3D/MERSI-II				MODIS			
Band ID	central wavelength (μm)	Bandwidth (nm)	Resolution (m)	SNR (K)	central wavelength (μm)	Bandwidth (nm)	Resolution (m)	SNR (K)
1	0.470	50	1000	100	0.469	20	500	243
2	0.550	50	1000	100	0.555	20	500	228
3	0.650	50	1000	100	0.645	50	500	128
4	0.865	50	1000	100	0.858	35	500	201
5	1.24/1.03	20	1000	100	1.240	20	500	74
6	1.640	50	1000	200	1.640	24	500	275
7	2.130	50	1000	100	2.130	50	500	110
FOV[1]	[-49.5°,49.5°]				[-55.04°, 55.04°]			

[1] FOV: Field of View

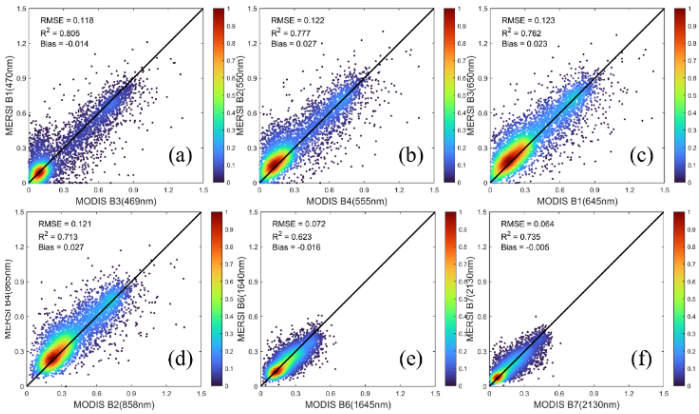

Fig. 2. Intercomparison between FY-3D MERSI-II surface reflectance and Aqua/Terra MODIS surface reflectance. The six subplots correspond to six MERSI-II spectral bands used for the intercomparison, containing bands 3 (0.470μm), 5 (0.550μm), 7 (0.650μm), 12 (0.865μm), 18 (1.640μm), and 19 (2.130μm).

C. *Landsat-8 FSC data*

The fractional snow cover derived from MERSI-II and MODIS was validated against Landsat-8 OLI imagery spanning China. Previous scholars have suggested that Landsat-8 images could be used as the reference dataset, as demonstrated through evaluation with Gaofen-2 panchromatic/multispectral (PMS) images [22]. Notably, the root mean square error (RMSE) of the Landsat-8 FSC was 0.094, underscoring the accuracy of this dataset. Fig. 1 shows the geographical spread of the validation dataset. Given that the 30-m spatial resolution data still contained mixed pixels, we implemented the MESMA-AGE algorithm. The Landsat-8/OLI FSC was computed on the Google Earth Engine (GEE) cloud computing platform [39]. This allowed us to quickly retrieve a total of 253 Landsat-8/OLI FSC images across China, of which the observed ground was partially or entirely covered with snow and not contaminated by clouds (a cloud cover less than 5%).

The endmember extraction rules for Landsat-8 OLI images (listed in TABLE II) proposed by previous research [22] was adopted in this study. After obtaining the 30-m OLI FSC images, pixels were aggregated and registered to be coincident with 1-km and 2-km MERSI-II FSC maps. The pixel aggregation has been used, and the formula as following:

$$FSC_{coarse} = \frac{\sum_N FSC_{finer,i} \times Area_{finer,i}}{Area_{coarse,i}} \quad (1)$$

Where FSC_{coarse} means FSC at a coarse scale, $FSC_{finer,i}$ represents FSC at a finer scale, N is the amount of fine pixels

contained in a coarse pixel, $Area_{finer,i}$ and $Area_{coarse,i}$ are area of fine pixels and coarse pixels, respectively.

TABLE II
RULES FOR EXTRACTING ENDMEMBERS FROM LANDSAT-8 OLI IMAGERY AND FY-3D MERSI-II IMAGERY [22]

Class	Rules (R_λ— surface reflectance at wavelength λ)	
	Landsat-8 OLI	FY-3D MERSI-II
Snow	NDVI[1] < -0.035, NDSI[2] > 0.75, $R_{0.55\mu m}$> 0.7	NDVI < -0.01, NDSI > 0.7, $R_{0.55\mu m}$ > 0.8, $R_{0.65\mu m}$ > 0.8, $R_{0.865\mu m}$ > 0.75
Vegetation	NDVI > 0.7, NDSI < -0.4, $R_{0.86\mu m}$ > 0.20	NDVI > 0.78, NDSI < -0.45, $R_{0.865\mu m}$ > 0.30
Soil/Rock	0 < NDVI < 0.15, NDSI < -0.4	-0.1 < NDVI < 0.15, NDSI < 0.15
Water	NDWI[3] > 0.2, $R_{0.86\mu m}$ < 0.2	NDWI > 0.4, $R_{0.865\mu m}$ < 0.3

[1] Normalized difference vegetation index (NDVI) is $(R_{NIR}-R_{RED})/(R_{RED}+R_{NIR})$.
[2] NDSI is $(R_{GREEN}-R_{SWIR})/(R_{GREEN}+R_{SWIR})$.
[3] Normalized difference water index (NDWI) [39] is $(R_{GREEN}-R_{NIR})/(R_{GREEN}+R_{NIR})$.

D. MODIS FSC data

The Terra/Aqua MODIS instruments offer a daily global coverage of the Earth's surface [40], with equatorial crossings at 10:30 and 13:30, while the MERSI-II instrument aboard FY-3D operates at 14:00. In this study, we used MOD09GA version 6 and MYD09GA version 6 as the MODIS inputs, which are available on the GEE cloud computing platform. TABLE I lists the spectral channel provided by MOD09GA. We fully leveraged the parallel computing capability of the GEE to calculate the MODIS FSC from January to February 2020, contemporaneous with the MERSI FSC. Although the daily Aqua overpass is temporally aligned with the FY-3D overpass, it lost 75% of its detectors for band 6 (1.640 μm), a crucial band for snow retrieval, shortly after its launch [41]. As a strategy for retrieving the MODIS-based FSC, Terra MODIS data were primarily considered, supplemented by Aqua MODIS data. The MESMA-AGE algorithm was implemented to generate 500-m snow cover maps from these MODIS datasets. And the endmember extraction rules for MODIS images are the same as those for MERSI-II images, which will be exhibited in section III.

E. The auxiliary data

The effects from different land-cover types and topography were considered when assessing snow fraction products. The GlobeLand30 product [42], provided by the Ministry of Natural Resources, was utilized as auxiliary data to account for the impact of various underlying surfaces on the generated FSC maps. In this work, the land cover types were consolidated into six categories, namely, water bodies, forests, grasslands, permanent snow and ice, croplands, and barren land. In addition, the Shuttle Radar Topography Mission (SRTM) digital elevation dataset spatially overlapping the study area was incorporated to conduct its topography effect on the snow fraction mapping method [43]. Fig. 1 shows the Land cover map and topographic relief in the study area.

III. SNOW COVER MAPPING ALGORITHM

Linear spectral mixing analysis that incorporates automatic extraction of endmembers was utilized to map FSC in China. The entire process of snow cover mapping can be divided into two parts: automatic endmember selection and multiple endmember spectral mixing analysis.

A. Endmember Selection Based on the Vector Length

According to previous research [16, 23], it is clear that even when all observed objects are confirmed to pertain to the same geophysical object, spectral reflectance discrepancies can still arise due to factors such as illumination and elevation. It is reasonable to implement spectral mixture analysis (SMA) based on multiple endmembers. In contrast to other MESMA algorithms, such as MODSCAG, the MESMA-AGE algorithm can be employed to automatically retrieve multigroup pure pixels, represented by different geophysical objects, from the whole image. The extraction rules for pure pixels are detailed in TABLE II. The optimization of the selection of endmembers for each land cover class must strike a balance between the computational efficiency and inversion accuracy. Cluster analysis was employed to extract representative endmembers from massive pixels. The method developed by [22, 44], which is based on the vector length of spectra, was adopted to retrieve representative endmembers. The vector length for spectral reflectance channels can be defined as follows:

$$\|r\| = \sqrt{\left(\sum_{k=1}^{N} r_k^2\right)} \tag{2}$$

where r_k is the reflectance of band k, and N is the number of bands. By arranging each group of endmembers in ascending order, we extracted typical endmembers at regular intervals from the sequence. In our study, we considered the research area as a complex field composed of vegetation, soil/rock, water, and snow cover parts. The extracted endmembers were accordingly classified into these four types.

B. Multiple Endmember Spectral Mixture Analysis

The MESMA-AGE algorithm operates under the assumption that each mixed pixel is a linear combination of the radiance reflected from individual surfaces, such as pure snow, vegetation, soil/rock, and water. Spectral mixture analysis can be implemented through a set of simultaneous linear equations that are solved to identify these individual components [21].

$$R_{mix,\lambda} = \sum_{i=1}^{N} F_i \cdot R_{i,\lambda} + \varepsilon_\lambda \quad (3)$$

$$\sum_{i=1}^{N} F_i = 1, i = 0,1, \dots, N \quad (4)$$

$$0 \le F_i \le 1, i = 0,1, \dots, N \quad (5)$$

where F_i is the fraction of endmember i; $R_{i,\lambda}$ is the reflectance of endmember i at wavelength λ; N is the number of bands; and ε_λ is the residual error at wavelength λ for the fit of the N endmembers.

This set of simultaneous linear equations can be effectively solved using the fully constrained least-squares fitting method. The precision of the mixture model, composed of various groups of endmembers, was quantified by the root mean square error (RMSE). Subsequently, the optimal group of endmembers is identified based on the minimum RMSE, enabling the determination of the fraction corresponding to each endmember.

IV. Validation and Comparison Metrics

In this work, the 1-km FSC aggregated from 30-m OLI images was considered the ground reference dataset to evaluate the precision of the calculated MERSI-II FSC. Considering that the MODIS fractional snow cover products produced by the MESMA-AGE algorithm have been demonstrated to be of high quality, we assessed the MERSI FSC against the MODIS FSC at the same spatial resolution. In this section, we introduce the evaluation metrics and comparison process.

The evaluation metrics used in previous validations of MODAGE, MOD10A1, and MODSCAG have been proven to be valuable for verifying the accuracy, overestimation, underestimation, and misestimation characteristics of these snow cover products [22].

To facilitate the comparison of reference and estimated data, we used a set of binary and fractional metrics. Assuming Landsat 8 snow cover maps to be the truth, pixels were classified into four possible outcomes for determining whether a pixel is snow or not: true positive (TP), true negative (TN), false-positive (FP), and false-negative (FN). The definitions of these four possible outcomes are provided in TABLE III. Given that the FSC exhibits a continuous value from 0 to 1, representing the ratio of the snow cover area in each pixel, the threshold for distinguishing snow pixels from snow-free pixels was defined as FSC = 0.15 [40]. If the FSC is less than 0.15, the pixel was classified as a snow-free pixel; otherwise, the pixel was regarded as a snow pixel.

TABLE III
CONTINGENCY TABLE OF BINARY SNOW IDENTIFICATION

Estimation FSC dataset	Reference FSC dataset	
	Snow	Snow-free
Snow	TP	FP
Snow-free	FN	TN

Common measures of the classification algorithm performance, calculated using the abovementioned four metrics (TP, TN, FP, and FN), include the following:

$$OA = \frac{TP + TN}{TP + TN + FP + FN} \quad (6)$$

$$UE = \frac{FN}{TP + FN} \quad (7)$$

$$OE = \frac{FP}{TN + FP} \quad (8)$$

where the overall accuracy (OA) indicates the overall detection precision, which is the probability that a pixel is correctly identified. The underestimation error (UE) measures the ratio of snow pixels that are mistakenly identified as non-snow pixels. The overestimation error (OE) measures the ratio of non-snow pixels mistakenly identified as snow pixels, with larger OE values indicating a more severe commission error.

Previous research [16, 22] has proposed the utilization of root mean square error (RMSE) as a metric to measure the performance of Snow cover mapping algorithms. The statistical measures were extended then with the addition of R^2, MAE, and Bias [40]. We utilized the root mean square error (RMSE), mean absolute error (MAE), R^2 and bias to estimate the accuracy of fractional snow cover estimation, which is a mathematically continuous variable. The metrics are defined as:

$$RMSE = \sqrt{\frac{1}{N}\sum_{i=1}^{N}\left(FSC_{est} - FSC_{ref}\right)^2} \quad (9)$$

$$MAE = \frac{\sum_{i=1}^{N}\left|FSC_{est} - FSC_{ref}\right|}{N} \quad (10)$$

$$R^2 = 1 - \frac{\sum_{i=1}^{N}\left(FSC_{est} - FSC_{ref}\right)^2}{\sum_{i=1}^{N}\left(FSC_{ref} - \overline{FSC_{ref}}\right)^2} \quad (11)$$

$$Bias = FSC_{est} - FSC_{ref} \quad (12)$$

where N is the total number of observations; FSC_{est} and FSC_{ref} denote the FSC values of pixels from the estimation and reference datasets, respectively, that share the same geolocation; and $\overline{FSC_{est}}$ is the mean value of FSC_{ref}. The RMSE is a measure of the deviation between the reference and estimated values but is sensitive to outliers. In addition, R^2 represents the goodness of fit, of which the value ranges from -1 to 1. The smaller the RMSE value is, along with a higher R^2 value, the higher the accuracy of the results.

To quantify the differences between paired observations of the MERSI and MODIS FSC results across different fractional snow cover values, we also introduced the bias box plot to offer a visual representation of misestimation (both overestimation and underestimation) for each interval.

V. RESULTS

In this study, we focused on mapping FSC from January to February since this period is the stable snow season and other seasons have less snowfall. Daily snow cover maps of China for

the period from January 1, 2020, to February 28, 2020, were generated. The MERSI-II FSC product can be considered as a near real-time product, for which the time for generating China FSC may be up to 3 min. Fig. 3 provides an overview on the behavior of daily FSC maps in the entire China region. In these daily contingency figures, the spatial consistency of FSC prediction is visually analyzed by comparing it with MERSI-II true-color RGB composite images. This band combination shows ice and snow in bright white, where water bodies and vegetations appear dark. As is shown in Fig. 3, the spatial distribution of snow is estimated precisely. To analyze the strengths and limitations of the FSC data, we used Landsat-8/OLI FSC as "Ground Truth". The evaluation dataset was then compared to this truth dataset at spatial resolutions of 1km and 2km, respectively. This aggregation at a coarser scale of 2km, as opposed to the 1-kilometer scale corresponding to MERSI-II's pixel size, aimed to minimize the uncertainty arising from spatial discrepancies in the imagery. Recognizing the unique characteristics of snow in areas with stable snow cover, it was deemed necessary to separately assess the snow cover maps of different regions. Additionally, the impact of underlying surfaces on the MERSI-II FSC was investigated in this study. The comparison of the MODIS and MERSI-II FSC results was also a significant part of this analysis.

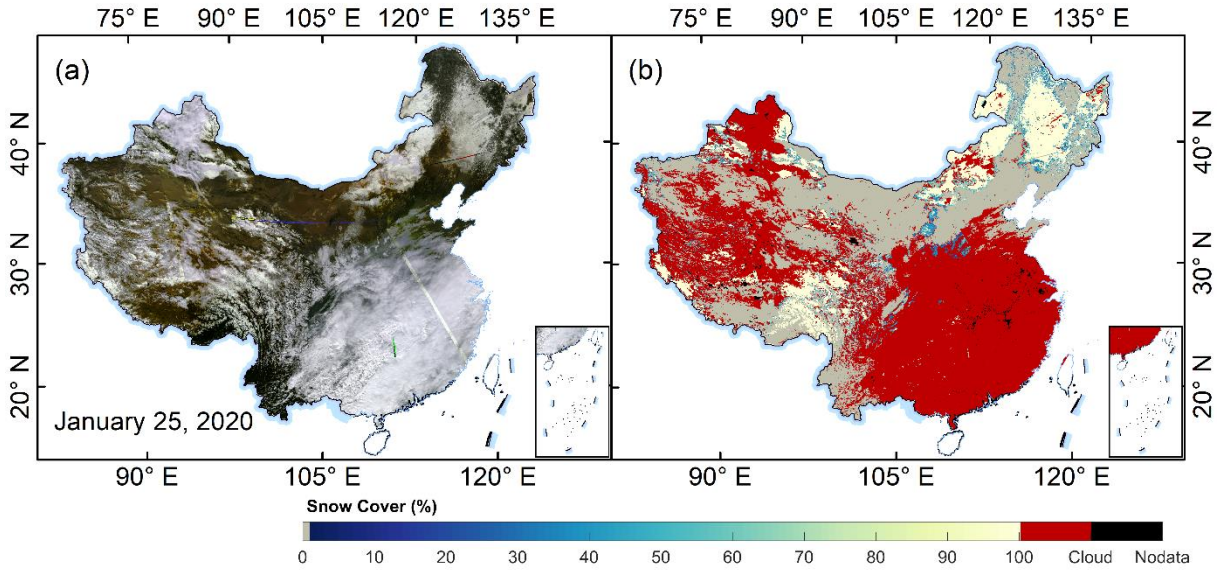

Fig. 3. Daily snow cover maps of the China retrieved from MERSI-II imagery on January 25, 2020. (a). FY-3D MERSI-II images. (b). The FSC map.

A. Fractional snow cover in China

TABLE IV presents a summary of the evaluation findings for the MERSI-II FSC, organized by different types of underlying surfaces. Research concluded that the aggregation process can eliminate the effect of geolocation error [15]. So, validation datasets at the 1-kilometer and 2-kilometer resolutions were generated.

TABLE IV
THE VALIDATION METRICS TO ASSESS FSC IN CHINA ACROSS DIFFERENT UNDERLYING SURFACES

Spatial Resolution		1 km			2 km		
Validation metrics		R^2	RMSE	MAE	R^2	RMSE	MAE
MODIS FSC	Forest	0.62	0.18	0.14	0.70	0.16	0.11
	Barren land	0.89	0.13	0.07	0.90	0.12	0.06
	Grassland	0.73	0.16	0.09	0.80	0.14	0.08
	Cropland	0.73	0.17	0.11	0.75	0.15	0.10
	All	0.80	0.16	0.10	0.84	0.14	0.08
MERSI-II FSC	Forest	0.42	0.23	0.16	0.48	0.20	0.15
	Barren land	0.93	0.11	0.05	0.94	0.10	0.05

Grassland	0.88	0.12	0.06	0.90	0.11	0.06
Cropland	0.83	0.16	0.09	0.86	0.14	0.09
All	0.86	0.15	0.08	0.88	0.13	0.07

The validation metrics revealed that the MESMA-AGE algorithm performs best in estimating FSC over barren land, with grasslands and croplands following closely. However, it encounters difficulties in accurately determining FSC over forested areas. The subpar performance in forest regions is likely due to a significant underestimation error. This inaccuracy may stem from the interference of forest canopies, which obstruct the view of snow on the ground. As a result, in alpine forest regions during winter, the primary electromagnetic information captured tends to emanate from the canopies and branches, rather than the snow-covered ground.

Furthermore, as is shown in TABLE IV, MODIS FSC outperforms MERSI-II FSC in forested regions. The reasons are as follows: First, variability in view geometry of MODIS and MERSI-II results in different accuracy in forested regions. Owing to obstruction of canopies, the viewable gap fraction (VGF) decreases. As view zenith decreases, the projected area of crown should decrease (i.e., you are seeing less of the side of a tree). Although similarity in scanning technology, the swath of MERSI-II (scanning angle ranges from −55.04° to 55.04°) is wider than MODIS (scanning angle ranges from -49.5° to 49.5°). More severe geometric distortion exists at the edges of the MERSI-II image, which might exacerbate MERSI-II's poor performance in forested areas. Second, spatial resolution is one of main impact factors that caused better performance of MODIS in the forested areas. MODIS, which has a 500 m nadir resolution is finer than MERSI-II. To eliminate the influence of view geometry and analyze only the effect due to spatial resolution, we compared FSC at nadir (View zenith angle varies from 0° to 5°) at the same resolution (1 km) by aggregating MODIS pixels. daily FSC maps from January to February 2020 were utilized. Only pixels from the Greater Khingan Range, where the forest is covered with snow, are analyzed. Landsat-8 OLI FSC is still chosen as the reference data. Fig. 4 shows the difference between accuracy of MODIS FSC and MERSI-II FSC at nadir. It demonstrates that spatial resolution plays an important role in explaining why MODIS outperforms MERSI in forested areas.

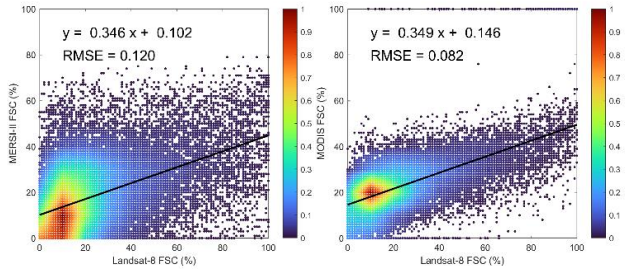

Fig. 4. Scatter plots of the MERSI-II (Left) and MODIS FSC (Right) versus Landsat-8 OLI FSC in the forested areas at nadir (View zenith angle varies from 0° to 5°)

The snow cover maps of China derived from MERSI-II imagery generally align well with the reference dataset, as evidenced by high R^2 values and low RMSE scores. Specifically at the grid-cell scale of 2-km, the FSC over barren land shows the lowest RMSE value of 0.10, with grasslands and croplands exhibiting similar accuracy. However, the accuracy diminishes in snow-covered forest areas, where the RMSE value reaches 0.20 and the R^2 value falls below 0.48. Slight improvement could be observed while spatial scale increased. It could be explained that coarser scale can decrease uncertainty arising from spatial discrepancies in the imagery. A comparison between the MODIS FSC and MERSI-II FSC data highlighted performance variations. While both datasets demonstrated comparable overall precision, they diverged in their accuracy across different FSC value ranges. This comprehensive analysis sheds light on the distinct advantages and limitations of different sensors, providing valuable insights for future enhancements and practical uses in snow cover mapping.

B. Fractional snow cover in Northeast China

This section illustrates the spatial distribution of FSC in Northeast China. Fig. 5(a) displays a remarkably homogenous and extensive snow cover across the southern-central Greater Khingan Range (A) and the Northeast China Plain (C). The Northeast China Plain is predominantly characterized by barren lands and grasslands. Since the radiance reflected from a combination of snow, grassland, and barren land surfaces can be effectively modeled as a single scattering system, which is apt for linear analysis [2], the FSC estimated in these spatial contexts exhibits high accuracy.

In Northeast China, the forest cover fraction is approximately 0.4. This widespread forest coverage introduces significant uncertainty in the retrieval of Fractional Snow Cover (FSC). A common issue in this study area is the underestimation of FSC at higher values. This inconsistency arises from the complexities inherent in forest environments, where the canopy can obscure the spectral information reflected by the snow-covered ground. As a result, mixed pixels in forested regions tend to represent the electromagnetic information from the canopies and branches more than the actual snow cover. This limitation highlights a challenge in using the MESMA-AGE algorithm for snow cover assessment in forested areas, underscoring the need for methodological refinements or additional data sources to improve accuracy in such areas [9, 35]. As is shown in Fig. 5, Regions I, II, and III are predominantly alpine forest areas. In these regions, the optical detectors of the MERSI-II satellite failed to accurately capture the electromagnetic information of the snow.

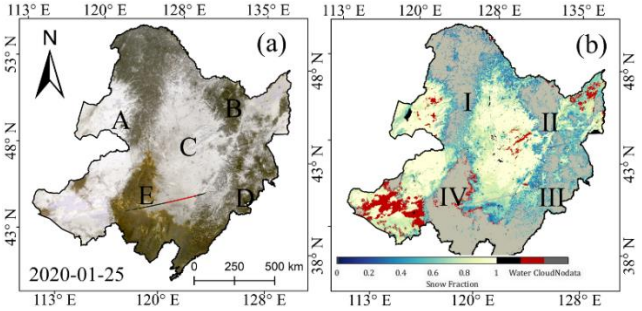

Fig. 5. True color map (a), FSC spatial distribution map (b) in the Northeast China on January 25, 2020. In subplot (a), the letters A to E represent Greater Khingan, Lesser Khingan, the Northeast China Plain, the Paektu Mountain, and the Horqin Sandy Land, respectively.

TABLE V details the validation metrics of FSC across varied underlying surfaces in Northeast China. Although the MERSI-II-based FSC demonstrates excellent capability in monitoring snow cover over barren lands, grasslands, and croplands, it notably underperforms in estimating snow cover within forested areas, indicated by a low R^2 value and a relatively high RMSE. Given the extensive spread of forests in Northeast China, this underestimation significantly impacts the overall effectiveness of the FSC assessment, resulting in less satisfactory outcomes.

TABLE V
THE VALIDATION METRICS TO ASSESS FSC IN THE NORTHEAST CHINA ACROSS DIFFERENT UNDERLYING SURFACES

Spatial Resolution		1 km			2 km		
Validation metrics		R^2	RMSE	MAE	R^2	RMSE	MAE
MODIS FSC	Forest	0.56	0.20	0.14	0.64	0.17	0.11
	Barren land	0.90	0.14	0.08	0.90	0.13	0.08
	Grassland	0.73	0.16	0.09	0.77	0.14	0.08
	Cropland	0.59	0.18	0.12	0.61	0.16	0.11
	All	0.77	0.17	0.11	0.82	0.15	0.10
MERSI-II FSC	Forest	0.20	0.11	0.17	0.23	0.21	0.16
	Barren land	0.94	0.11	0.10	0.94	0.10	0.05
	Grassland	0.88	0.11	0.05	0.90	0.10	0.05
	Cropland	0.75	0.17	0.10	0.79	0.15	0.10
	All	0.81	0.17	0.10	0.84	0.15	0.09

C. Fractional snow cover on the Tibetan Plateau

The Tibetan Plateau, often termed the "Third Pole," exhibits a distinct and intricate snow cover pattern. Positioned at an average altitude surpassing 4000 meters, snow cover in this region is characteristically sporadic in the mountainous zones and sparse in the inland plateau areas [24]. Research such as [45] has shown that snow cover tends to be more persistent in the southeastern, western, and southern parts of the Tibetan Plateau. Despite the frequency of snowfall in winter, atmospheric conditions like low vapor content leads to a patchy and thin snow layer on the plateau. Nevertheless, numerous studies have effectively utilized the MESMA-AGE algorithm for precise estimation of FSC in this region [22-24]. In this study, we evaluated the performance of the FY-3D MERSI-II FSC on the Tibetan Plateau and validated it against 70 Landsat-8 OLI FSC scenes. This comparative analysis reinforces the notion that the MERSI-II and MESMA-AGE algorithm are valuable tools for detailed snow cover analysis in this geographically complex and critically important region.

The MERSI-II FSC assessment of the Tibetan Plateau has yielded encouraging results in mapping its complex snow cover patterns. As shown in TABLE VI, MERSI-II has an RMSE of 0.10 and an R^2 value of 0.95 at 2 km resolution. FSC measurements in barren land areas showed the most accurate results. However, the extraction of FSC in forested areas remains challenging, aligning with findings in previous sections that emphasized the interference of forest canopies in snow detection. In areas where snow cover is spatially extensive and forest coverage is minimal, MERSI-II effectively provides precise FSC estimations. The accuracy of results for croplands and grasslands falls in the intermediate range, positioned between the performances in barren and forested terrains.

TABLE VI
THE VALIDATION METRICS TO ASSESS FSC OVER THE TIBETAN PLATEAU ACROSS DIFFERENT UNDERLYING SURFACES

Spatial Resolution		1 km			2 km		
Validation metrics		R^2	RMSE	MAE	R^2	RMSE	MAE
MODIS FSC	Forest	0.85	0.13	0.06	0.88	0.12	0.06
	Barren land	0.89	0.11	0.05	0.91	0.10	0.05
	Grassland	0.82	0.15	0.09	0.88	0.12	0.07
	Cropland	0.86	0.11	0.04	0.89	0.08	0.02
	All	0.90	0.13	0.07	0.93	0.11	0.06
MERSI-II FSC	Forest	0.73	0.18	0.09	0.78	0.16	0.09
	Barren land	0.95	0.08	0.03	0.95	0.08	0.03
	Grassland	0.94	0.11	0.04	0.95	0.10	0.04
	Cropland	0.81	0.11	0.04	0.85	0.10	0.04
	All	0.94	0.11	0.04	0.95	0.10	0.04

In conclusion, the snow cover maps generated from MERSI-II images for the Tibetan Plateau demonstrate remarkable consistency across various underlying surfaces, surpassing the performance observed in other regions with stable snow cover.

D. Fractional snow cover in northern Xinjiang

Xinjiang, located in the arid and semi-arid regions of Central Asia, grapples with a notable scarcity of freshwater resources. In this area, surface runoff predominantly originates from the melting of mountain glaciers and snow cover [46]. Notably, Northern Xinjiang stands as China's most abundant region in terms of seasonal snow-water resources, contributing about one-third of the country's snow resources [47]. With an average annual precipitation of 244 mm [48], Northern Xinjiang extends from 42° to 50°N and from 79° to 92°E, as depicted in Fig. 6 (a)), and is flanked by the Tianshan and Altai Mountains.

TABLE VII reveals that, according to the validation metrics, the MERSI-II Fractional Snow Cover (FSC) surpassed the performance of MODIS FSC. Among various underlying surfaces, the FSC in forested areas showed the least favorable results, with an R^2 value of 0.51 and an RMSE of 0.20 at the grid-cell scale of 2-km. In contrast, the FSC over barren land demonstrated the most accurate performance, featuring an R^2 value of 0.94 and an RMSE of 0.10.

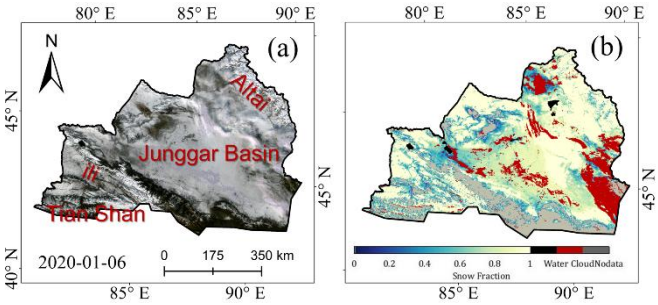

Fig. 6. True color map (a), FSC spatial distribution map (b) in the Northeast China on January 6, 2020.

TABLE VII
THE VALIDATION METRICS TO ASSESS MERSI-II FSC OF NORTHERN XINJIANG ACROSS DIFFERENT UNDERLYING SURFACES

Spatial Resolution		1 km			2 km		
Validation metrics		R^2	RMSE	MAE	R^2	RMSE	MAE
MODIS FSC	Forest	0.49	0.18	0.12	0.58	0.15	0.10
	Barren land	0.87	0.14	0.08	0.89	0.13	0.07
	Grassland	0.59	0.18	0.10	0.76	0.13	0.08
	Cropland	0.36	0.17	0.09	0.58	0.12	0.07
	All	0.79	0.16	0.09	0.85	0.13	0.08
MERSI-II FSC	Forest	0.46	0.23	0.16	0.51	0.20	0.15
	Barren land	0.93	0.12	0.06	0.94	0.10	0.05

Grassland	0.80	0.15	0.09	0.83	0.14	0.08
Cropland	0.86	0.12	0.06	0.89	0.11	0.06
All	0.89	0.13	0.07	0.90	0.12	0.07

Researchers have reported that the mapping accuracy is influenced by the variable illumination, which is caused by the complex topography [28, 49]. Fig. 6 and Fig. 7 highlight that the Altai Mountains, Junggar Basin, and Tianshan Mountains are the primary geographical subregions in this context. In this study, 41 Landsat-8/OLI FSC images were categorized into three groups corresponding to these geographical subregions. Fig. 7 illustrates the distribution of Landsat-8/OLI scenes and the validation metrics for these areas. The boxplots of RMSE and R^2 values indicate that the suboptimal performance of FSC over the Tianshan Mountains was a significant contributor to the increased overall error in snow cover mapping across northern Xinjiang. Among these three subregions, the snow cover maps for the Junggar Basin exhibited the most accurate results.

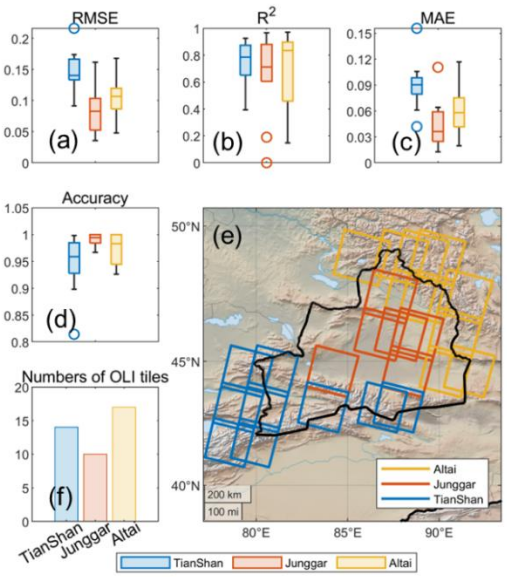

Fig. 7. Validation metrics calculated from MERSI-II FSC imagery over different terrain areas of the Northern Xinjiang.

In conclusion, the accuracy of snow cover mapping over northern Xinjiang is notable, demonstrating a considerable level of success for the different underlying surfaces. We conducted an extensive evaluation of FSC across varied landscapes. The FSC accuracy was highest over barren land areas, while forest regions displayed the lowest accuracy. Furthermore, the study identified terrain-induced errors specific to this area. By analyzing FSC performance across the three distinct geographical subregions, it was concluded that the complex terrain of the Tianshan Mountains played a significant role in increasing the overall error in northern Xinjiang. This outcome highlights the complex interaction between topography, land cover, and remote sensing technologies. It emphasizes the necessity of accounting for these factors to achieve more precise snow cover mapping in diverse geographical settings.

VI. Discussion

In this study, we showcased the robust capabilities of the MERSI-II instrument aboard the FY-3D satellite for monitoring snow cover throughout China's snow season. This section delves into evaluating the performance of FSC estimation across different snow regions. Additionally, we scrutinize the challenges faced in snow cover mapping, especially in forested regions and areas with complex terrain. Moreover, we offer a comparative analysis of the MERSI-II FSC, MODIS FSC, and MULSS Snow Cover products, highlighting their respective strengths and areas for improvement. We focused on mapping FSC from January to February since this period is the stable snow season and other seasons have less snowfall.

A. Performance of FSC estimation in various snow regions

Fig. 8 illustrates the bias distributions in coarse-scale FSC datasets (MERSI-II and MODIS) compared to the Landsat-8/OLI FSC datasets across China and three primary stable snow-covered areas. The FSC pixels were categorized into 11 groups, ranging from 0 to 1, and evaluated based on bias. The biases in the MERSI-II FSC are more widely spread than those in the MODIS product, particularly in the range of [0.15, 0.75]. This suggests that MERSI-II is less consistent with the Landsat-8/OLI FSC, indicating higher uncertainty. In other FSC ranges, the MERSI-II FSC shows minor systematic misestimation. Additionally, the MERSI-II FSC demonstrates a slight negative bias in the range of [0.05, 0.35] and a positive bias in the range of [0.65, 0.95]. This pattern indicates a tendency to underestimate in areas with low FSC values and overestimate in those with high FSC values. Conversely, the biases in the MODIS FSC are negatively concentrated for FSC values greater than 0.8, implying systematic underestimation in MODIS-derived FSC retrieval. Overall, the MERSI-II instrument is more effective for extracting FSC in areas with high FSC values, whereas MODIS is better suited for low or moderate FSC values. The differing performance levels can be attributed to two main factors: firstly, the aging MODIS instruments experience detector and optical system degradation [50] , while MERSI-II remains more effective in snowfields. Secondly, the atmospheric correction method [27, 51] used in MERSI-II surface reflectance products is better suited for bright surfaces like snow, enhancing the accuracy of FSC extraction in stable snow-covered areas compared to darker surfaces.

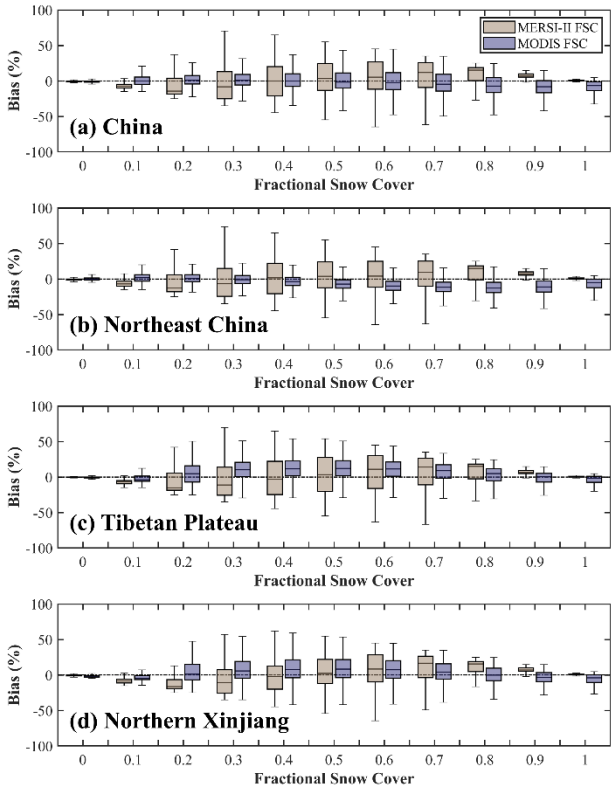

Fig. 8. Different behaviors of snow cover maps retrieved from MODIS and MERSI-II imageries of China, compared with Landsat-8 OLI FSC

B. Limitations of snow cover mapping in forested areas

The validation results for the FSC in forest areas across all geographical regions varied, particularly in Northeast China. The complexity of the three-dimensional structure of forests results in challenges in detecting snow cover. Owing to obstruction of canopies, widespread underestimation could be observed in the alpine forests. Diffuse radiation reaching the snow surface is reduced, which is caused by trees shielding the sky hemisphere [52, 53]. At the level of tree stands, previous research [54] has demonstrated differences between snow across forest edges of different distances and orientation. Also, snow distribution is strongly correlated to open fraction of canopies at the grid-cell level (20-200m scale). with coarser spatial resolution, optical sensors with medium and coarse resolutions are designed to have the oblique perspective and large field of view. At the coarse grid-cell level, the viewable gap fraction (VGF) decreases and the pixels are stretched as the viewing zenith angle (VZA) decreases because vertical features like trees become projected [55]. Hence, accurate monitoring of the snow cover requires highly sensitive sensors that can detect details through gaps in the forests. However, MERSI-II detectors are hindered by their coarse resolution, making it difficult to capture the spectrum of snow.

C. Limitation of snow cover mapping in complex terrain

The complex topography results in varying illumination conditions, which in turn impacts the accuracy of mapping. For example, the intricate terrain of the TianShan Mountains, as shown in Fig. 7, contributes to an increased overall error in the northern Xinjiang region. This scenario highlights the influence of topographical elements on the precise retrieval of Fractional Snow Cover (FSC), demonstrating how terrain complexity can pose challenges to accurate snow cover mapping.

The use of multiple endmembers in spectral mixture analysis, despite its advancements, still faces challenges in mitigating the adverse effects of complex terrain [11]. This section focuses on presenting statistical accuracy metrics for FSC in relation to terrain slope. The slope data was derived from the Shuttle Radar Topography Mission (SRTM) Digital Elevation Model (DEM) dataset. Fig. 9 displays the R^2 and RMSE values for the MERSI-II FSC across China and the three major stable snow-covered areas. In China, FSC shows optimal performance in areas with slopes ranging from 0° to 30°, as evidenced by high R^2 values and low RMSE values. However, beyond a 30° slope, a significant drop in accuracy could be observed. Steep terrain introduces factors like altered illumination and shadowing, which greatly increase the uncertainty in spectral mixture analysis. For Northeast China and the Tibetan Plateau, as illustrated in Fig. 9, both R^2 and RMSE values exhibit a notable increase with steeper slopes. Despite Northeast China's relatively flat topography, the accuracy metrics display significant variability. This is largely attributed to forested areas in high-altitude regions like the Greater Khingan, Lesser Khingan, and Paektu Mountain, which add to the complexity of accurately retrieving snow cover data. In Northern Xinjiang, R^2 values show relative consistency for slopes between 0° and 25°, but lower values occur over 26°. While RMSE values generally remain low across different slopes, there is a pronounced increase between 26° and 30°, indicating heightened uncertainty in steep areas. In summary, the statistical validation metrics quantitatively demonstrate that while the MERSI-II FSC is effective in monitoring snow cover in flat terrains, its performance is significantly compromised in steep terrains. This highlights the importance of considering terrain slope as a critical factor in snow cover mapping and the need for algorithmic improvements or complementary methods to enhance accuracy in complex terrains.

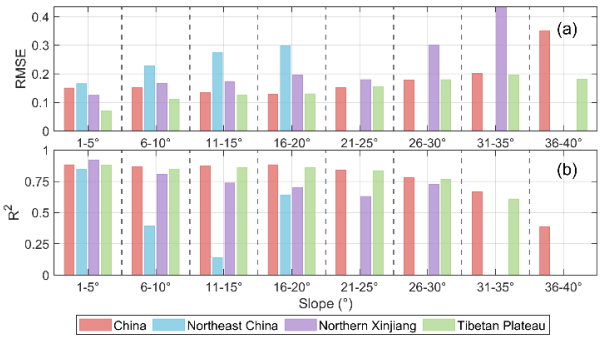

Fig. 9. The statistic validation metrics of MERSI-II FSC as they vary with terrain slope

D. Differences between MERSI-II FSC and MULSS snow cover products

The accessible MULSS daily maximum Snow Cover (SNC) products provided by the NSMC offer daily identification and integration of VIRR and MERSI multiorbit maximum snow cover data retrieved from FY-3A and FY-3C satellites with a resolution of 0.01°. In contrast to the more detailed fractional snow cover products, SNC products employ

a binary classification, dividing images into snow and snow-free pixels. This resolution of 0.01° (approximately 1 km) indicates that mixed pixels are present, and the binary classification algorithm of the SNC products lacks the capacity to provide finer-scale snow cover information. In this study, performances of three different snow-cover maps (MERSI-II FSC, MODIS FSC, and SNC products) on classifying pixels as snow or non-snow, were compared with Landsat-8 OLI FSC, respectively. The OA, OE, and UE metrics were used to assess the precision of these three products. Given that the fractional snow cover retrieved from MERSI-II and MODIS is a continuous value from 0 to 1, representing the snow cover fraction in each pixel, the threshold for classifying a pixel as a snow or snow-free pixel was defined as FSC = 0.15. TABLE VIII provides a summary of the binary assessment results. At the grid-cell scale of 2km, the overall accuracy (OA) of the MERSI-II FSC, MODIS FSC and MULSS SNC was 0.93, 0.96, and 0.91, respectively. MODIS FSC and MULSS SNC overestimate the results and lead to generate high OE values. According to effects of different underlying surfaces, all of three products perform well for snow cover over barren land, grasslands and, croplands. These OA values indicate that the MODIS product could identify snow pixels most accurately. However, larger deviations can be observed in results over forests. While underestimation is prominent for MERSI-II FSC and MODIS FSC, MULSS SNC shows an underestimation of distinguishing snow and snow-free pixels. It can be explained that the strategies adopted in the MULSS algorithm which are similar to the SNOMAP algorithm [26] lead to significant overestimation of the product in forest areas. This observation highlights the inherent limitations of binary classification in capturing the nuanced variation in the snow cover, especially on finer scales. While binary classification provides a more straightforward representation of snow presence, it may lack the detail and accuracy needed for certain applications. The comparison between the MERSI-II FSC and MULSS SNC products emphasizes the importance of considering the methods, algorithms, and resolutions used in snow cover mapping to achieve the desired level of accuracy and detail in various environmental and climatological studies.

TABLE VIII
SUMMARY OF THE BINARY STATISTICS

Spatial Resolution		1km			2km		
Validation metrics		OE	UE	OA	OE	UE	OA
MERSI-II FSC	Forest	0.16	0.27	0.78	0.12	0.28	0.79
	Barren land	0.02	0.06	0.95	0.01	0.06	0.95
	Grassland	0.04	0.03	0.97	0.02	0.03	0.97
	Cropland	0.04	0.04	0.96	0.02	0.05	0.96
	All	0.07	0.07	0.93	0.05	0.07	0.93
MODIS FSC	Forest	0.06	0.3	0.85	0.06	0.22	0.88
	Barren land	0.02	0.03	0.97	0.01	0.03	0.97
	Grassland	0.08	0.01	0.98	0.02	0.01	0.99
	Cropland	0.06	0.01	0.98	0.02	0.01	0.98
	All	0.02	0.15	0.96	0.10	0.02	0.96
MULSS SNC	Forest	0.38	0.17	0.75	0.35	0.17	0.76
	Barren land	0.03	0.11	0.91	0.02	0.10	0.92
	Grassland	0.08	0.08	0.91	0.06	0.07	0.93
	Cropland	0.04	0.06	0.94	0.04	0.05	0.95
	All	0.13	0.09	0.89	0.11	0.08	0.91

E. Performance of MERSI-II FSC during the snowmelt season

In this study, we focused on mapping FSC only during the winter season because little snowfall is observed within China during the other seasons. But the performance of MERSI-II during the snow-melt season is discussed in this section. We retrieved FSC in China from March 1 to May 7, 2020 as a supplement. Another 85 Landsat-8/OLI FSC images were retrieved as a reference dataset. Fig. 10 shows RMSE and R^2 of MERSI-II FSC from January, 2020 to April, 2020. Slight reduction of accuracy can be seen when comparing RMSE during the snowmelt season (March, 2020 and April, 2020) with that during the snowfall season. It is owing to the fragmented and thin snow distribution exacerbating the uncertainty of retrieval in this period. Nevertheless, the performance of the MESMA-AGE algorithm during this period is very similar to that in the snow season.

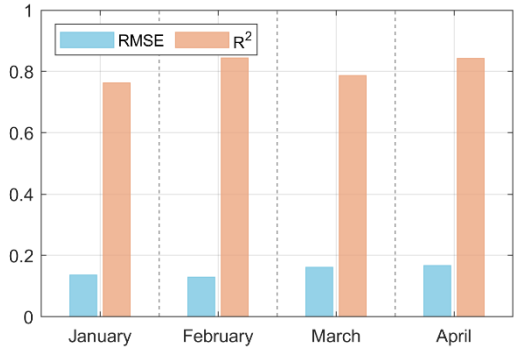

Fig. 10. Monthly statistic validation metrics of MERSI-II FSC

VII. Conclusion

The MERSI-II sensor aboard the FY-3D satellite has been utilized for snow cover monitoring across China. The MESMA-AGE algorithm was applied for snow cover mapping with the FY-3D/MERSI-II sensor. Four surface types including soil, snow, vegetation, and water are considered in estimate of snow area in each pixel. In this study, daily MERSI-II snow cover maps from January 1, 2020, to February 28, 2020, were produced and validated against finer-scale OLI-derived FSC. The results demonstrate the MERSI-II instrument's capability for daily, extensive-scale snow cover monitoring. Enhanced by improved endmember representation and automated processing, this FSC mapping method shows commendable performance in China. Notably, MERSI-II achieved an RMSE of 0.13 and an R^2 value of 0.88 when validated versus 253 OLI-based FSC scenes. It exhibits a slight edge over MODIS, partly due to the aging of MODIS instruments leading to reduced performance in monitoring variations over snowpacks. Additionally, the atmospheric correction method used for MERSI-II surface reflectance datasets [51] is particularly effective for bright surfaces like snow. Further assessments revealed consistent accuracy in estimating FSC in barren land areas across all geographical subregions. Grasslands and croplands, however, showed less optimal results compared to barren lands. A significant concern is the underestimation of FSC in forested areas, where canopy cover can hinder the detection of spectral information from snow. This issue leads to notable uncertainties in FSC mapping. In this work, forest as the main vegetation type in winter was considered on a horizontal scale. However, in the vertical direction, the impact of forests on mapping OLI FSC was not considered. The study also evaluated snow cover mapping accuracy in three major snow cover regions: the Tibetan Plateau, northern Xinjiang, and Northeast China. The Tibetan Plateau and northern Xinjiang, with their extensive bare surfaces and alpine meadows, showed superior precision in snow cover mapping. In contrast, Northeast China, with a fractional forest cover over 0.4, exhibited the least accuracy. Terrain impacts were also observed, indicating that MERSI-II FSC is effective in flat terrains but less so in steep areas. Future efforts will aim to enhance the snow cover mapping algorithm for alpine forests and steep terrain.

References

[1].Flanner, M. G., et al., "Radiative forcing and albedo feedback from the Northern Hemisphere cryosphere between 1979 and 2008", *Nature Geoscience*, vol 4, no. 3, pp.151-155, 2011, doi: 10.1038/ngeo1062.

[2].Rohrer, M., et al., "Missing (in-situ) snow cover data hampers climate change and runoff studies in the Greater Himalayas", *Sci Total Environ*, vol 468-469 Suppl, no., pp.S60-70, 2013, doi: 10.1016/j.scitotenv.2013.09.056.

[3].Dedieu, J. P., et al., "Shifting mountain snow patterns in a changing climate from remote sensing retrieval", *Sci Total Environ*, vol 493, no., pp.1267-1279, 2014, doi: 10.1016/j.scitotenv.2014.04.078.

[4].Jiang, L., et al., "Progress on Remote Sensing of Snow, Surface Soil Frozen/Thaw State and Soil Moisture", *Remote Sensing Technology and Application*, vol 35, no. 06, pp.1237-1262, 2020, doi: 10.11873/j.issn.1004-0323.2020.6.1237.

[5].Gao, J., "Analysis and assessment of the risk of snow and freezing disaster in China", *International Journal of Disaster Risk Reduction*, vol 19, no., pp.334-340, 2016, doi: 10.1016/j.ijdrr.2016.09.007.

[6].Salomonson, V. V. and I. Appel, "Estimating fractional snow cover from MODIS using the normalized difference snow index", *Remote Sensing of Environment*, vol 89, no. 3, pp.351-360, 2004, doi: 10.1016/j.rse.2003.10.016.

[7].Dozier, J., "Spectral signature of alpine snow cover from the landsat thematic mapper", *Remote Sensing of Environment*, vol 28, no., pp.9-22, 1989, doi: https://doi.org/10.1016/0034-4257(89)90101-6.

[8].Wang, G., et al., "A Universal Ratio Snow Index for Fractional Snow Cover Estimation", *IEEE Geoscience and Remote Sensing Letters*, vol 18, no. 4, pp.721-725, 2021, doi: 10.1109/lgrs.2020.2982053.

[9].Wang, X., et al., "An Adaptive Snow Identification Algorithm in the Forests of Northeast China", *IEEE Journal of Selected Topics in Applied Earth Observations and Remote Sensing*, vol 13, no., pp.5211-5222, 2020, doi: 10.1109/jstars.2020.3020168.

[10].Wang, G., et al., "Characterization of NDSI Variation: Implications for Snow Cover Mapping", *IEEE Transactions on Geoscience and Remote Sensing*, vol 60, no., pp.1-18, 2022, doi: 10.1109/tgrs.2022.3165986.

[11].Czyzowska-Wisniewski, E. H., et al., "Fractional snow cover estimation in complex alpine-forested environments using an artificial neural network", *Remote Sensing of Environment*, vol 156, no., pp.403-417, 2015, doi: 10.1016/j.rse.2014.09.026.

[12].Hou, J., et al., "On the Value of Available MODIS and Landsat8 OLI Image Pairs for MODIS Fractional Snow Cover Mapping Based on an Artificial Neural Network", *IEEE Transactions on Geoscience and Remote Sensing*, vol 58, no. 6, pp.4319-4334, 2020, doi: 10.1109/tgrs.2019.2963075.

[13].Dobreva, I. D. and A. G. Klein, "Fractional snow cover mapping through artificial neural network analysis of MODIS surface reflectance", *Remote Sensing of Environment*, vol 115, no. 12, pp.3355-3366, 2011, doi: 10.1016/j.rse.2011.07.018.

[14].Kuter, S., "Completing the machine learning saga in fractional snow cover estimation from MODIS Terra reflectance data: Random forests versus support vector regression", *Remote Sensing of Environment*, vol 255, no., 2021, doi: 10.1016/j.rse.2021.112294.

[15].Painter, T. H., et al., "Retrieval of subpixel snow covered area, grain size, and albedo from MODIS", *Remote Sensing of Environment*, vol 113, no. 4, pp.868-879, 2009, doi: 10.1016/j.rse.2009.01.001.

[16].Shi, J., "An automatic algorithm on estimating sub-pixel snow cover from MODIS", *Quat. Sci*, vol 32, no. 01, pp.6-15, 2012, doi: 10.1016/j.rse.2017.01.023.

[17].Dozier, J., et al., "Mapping alpine snow using a spectral mixture modeling technique", *Annals of Glaciology*, vol 17, no., pp.121-124, 1993, doi: 10.3189/S0260305500012702.

[18].Klein, A. G. and B. L. Isacks, "Spectral mixture analysis of Landsat thematic mapper images applied to the detection of the transient snowline on tropical Andean glaciers", *Global and*

Planetary Change, vol 22, no., pp.139-154, 1999, doi: 10.1016/s0921-8181(99)00032-6.

[19].Vikhamar, D. and R. Solberg, "Snow-cover mapping in forests by constrained linear spectral unmixing of MODIS data", *Remote Sensing of Environment*, vol 88, no. 3, pp.309-323, 2003, doi: 10.1016/j.rse.2003.06.004.

[20].Kerekes, J. P. and J. E. Baum, "Spectral imaging system analytical model for subpixel object detection", *IEEE Transactions on Geoscience and Remote Sensing*, vol 40, no., pp.1088-1101, 2002, doi: 10.1109/tgrs.2002.1010896.

[21].Roberts, D. A., et al., "Mapping Chaparral in the Santa Monica Mountains Using Multiple Endmember Spectral Mixture Models", *Remote Sensing of Environment*, vol 65, no., pp.267-279, 1998, doi: 10.1016/s0034-4257(98)00037-6.

[22].Hao, S., et al., "Assessment of MODIS-Based Fractional Snow Cover Products Over the Tibetan Plateau", *IEEE Journal of Selected Topics in Applied Earth Observations and Remote Sensing*, vol 12, no. 2, pp.533-548, 2019, doi: 10.1109/jstars.2018.2879666.

[23].Zhu, J., et al., "Subpixel Snow Mapping Using Daily AVHRR/2 Data over Qinghai–Tibet Plateau", *Remote Sensing*, vol 14, no. 12, 2022, doi: 10.3390/rs14122899.

[24].Wang, G., et al., "Fractional Snow Cover Mapping from FY-2 VISSR Imagery of China", *Remote Sensing*, vol 9, no. 10, 2017, doi: 10.3390/rs9100983.

[25].Pan, F., et al., "Retrieval of Fractional Snow Cover over High Mountain Asia Using 1 km and 5 km AVHRR/2 with Simulated Mid-Infrared Reflective Band", *Remote Sensing*, vol 14, no. 14, 2022, doi: 10.3390/rs14143303.

[26].Yang, J., et al., "Monitoring snow cover using Chinese meteorological satellite data over China", *Remote Sensing of Environment*, vol 143, no., pp.192-203, 2014, doi: 10.1016/j.rse.2013.12.022.

[27].Zhong, B., et al., "An Atmospheric Correction Method over Bright and Stable Surfaces for Moderate to High Spatial-Resolution Optical Remotely Sensed Imagery", *Remote Sensing*, vol 12, no. 4, 2020, doi: 10.3390/rs12040733.

[28].Huang, X., et al., "Spatiotemporal dynamics of snow cover based on multi-source remote sensing data in China", *The Cryosphere*, vol 10, no. 5, pp.2453-2463, 2016, doi: 10.5194/tc-10-2453-2016.

[29].Gao, Y., et al., "Contrasting changes of snow cover between different regions of the Tibetan Plateau during the latest 21 years", *Frontiers in Earth Science*, vol 10, no., 2023, doi: 10.3389/feart.2022.1075988.

[30].Li, X., et al., "Snow cover classification based on climate variables and its distribution characteristics in China", *Journal of Glaciology and Geocryology*, vol 42, no. 01, pp.62-71, 2020, doi.

[31].Ma, Y., et al., "Atmospheric moisture transport versus precipitation across the Tibetan Plateau: A mini-review and current challenges", *Atmospheric Research*, vol 209, no., pp.50-58, 2018, doi: 10.1016/j.atmosres.2018.03.015.

[32].Liu, X., et al., "Large-Scale Dynamics and Moisture Sources of the Precipitation Over the Western Tibetan Plateau in Boreal Winter", *Journal of Geophysical Research: Atmospheres*, vol 125, no. 9, 2020, doi: 10.1029/2019jd032133.

[33].Guangrui, W., et al., "An investigation on microwave transmissivity at frequencies of 18.7 and 36.5 GHz for diverse forest types during snow season", *International Journal of Digital Earth*, vol 14, no. 10, pp.1354-1379, 2021, doi: 10.1080/17538947.2021.1955985.

[34].Che, T., et al., "Estimation of snow depth from passive microwave brightness temperature data in forest regions of northeast China", *Remote Sensing of Environment*, vol 183, no., pp.334-349, 2016, doi: 10.1016/j.rse.2016.06.005.

[35].Shen, X., et al., "Spatiotemporal variation in vegetation spring phenology and its response to climate change in freshwater marshes of Northeast China", *Sci Total Environ*, vol 666, no., pp.1169-1177, 2019, doi: 10.1016/j.scitotenv.2019.02.265.

[36].Yunyu, Z., et al., "FY-3D/MERSI-II Meteorological Satellite Image Fusion Method and its Application", *2020 IEEE 3rd International Conference on Information Systems and Computer Aided Education (ICISCAE)*, vol, no., pp.237-240, 2020, doi: 10.1109/ICISCAE51034.2020.9236890.

[37].Xu, N., et al., "Prelaunch Calibration and Radiometric Performance of the Advanced MERSI II on FengYun-3D", *IEEE Transactions on Geoscience and Remote Sensing*, vol 56, no. 8, pp.4866-4875, 2018, doi: 10.1109/tgrs.2018.2841827.

[38].Han, X., et al., "Fengyun-3D MERSI True Color Imagery Developed for Environmental Applications", *Journal of Meteorological Research*, vol 33, no. 5, pp.914-924, 2019, doi: 10.1007/s13351-019-9028-7.

[39].McFeeters, S. K., "The use of the Normalized Difference Water Index (NDWI) in the delineation of open water features", *International Journal of Remote Sensing*, vol 17, no. 7, pp.1425-1432, 2007, doi: 10.1080/01431169608948714.

[40].Rittger, K., et al., "Evaluation of VIIRS and MODIS Snow Cover Fraction in High-Mountain Asia Using Landsat 8 OLI", *Frontiers in Remote Sensing*, vol 2, no., 2021, doi: 10.3389/frsen.2021.647154.

[41].Gladkova, I., et al., "Quantitative Restoration for MODIS Band 6 on Aqua", *IEEE Transactions on Geoscience and Remote Sensing*, vol 50, no. 6, pp.2409-2416, 2012, doi: 10.1109/tgrs.2011.2173499.

[42].Shi, X., et al., "Application and impacts of the GlobeLand30 land cover dataset on the Beijing Climate Center Climate Model", *IOP Conference Series: Earth and Environmental Science*, vol 34, no., 2016, doi: 10.1088/1755-1315/34/1/012032.

[43].Tadono, T., et al., "Precise Global DEM Generation by ALOS PRISM", *ISPRS Annals of the Photogrammetry, Remote Sensing and Spatial Information Sciences*, vol II-4, no., pp.71-76, 2014, doi: 10.5194/isprsannals-II-4-71-2014.

[44].Xu, Y., et al., "An Improved Endmember Selection Method Based on Vector Length for MODIS Reflectance Channels", *Remote Sensing*, vol 7, no. 5, pp.6280-6295, 2015, doi: 10.3390/rs70506280.

[45].Yang, J., et al., "Evaluation of snow products over the Tibetan Plateau", *Hydrological Processes*, vol 29, no. 15, pp.3247-3260, 2015, doi: 10.1002/hyp.10427.

[46].Cohen, J. and D. Entekhabi, "Eurasian snow cover variability and northern hemisphere climate predictability", *Geophysical Research Letters*, vol 26, no. 3, pp.345-348, 1999, doi: 10.1029/1998gl900321.

[47].Li, P., "Preliminary evaluation of seasonal snow resources in China", *Acta Geographica Sinica*, vol 43, no. 02, pp.108-119, 1988, doi.

[48].Ke, C. Q. and X. Liu, "MODIS-observed spatial and temporal variation in snow cover in Xinjiang, China", *Climate Research*, vol 59, no. 1, pp.15-26, 2014, doi: 10.3354/cr01206.
[49].Tang, Z., et al., "Spatiotemporal Variation of Snow Cover in Tianshan Mountains, Central Asia, Based on Cloud-Free MODIS Fractional Snow Cover Product, 2001–2015", *Remote Sensing*, vol 9, no. 10, 2017, doi: 10.3390/rs9101045.
[50].Xiong, X., et al., "MODIS Reflective Solar Bands On-Orbit Calibration and Performance", IEEE Transactions on Geoscience and Remote Sensing, vol 57, no. 9, pp.6355-6371, 2019, doi: 10.1109/tgrs.2019.2905792.
[51].Liang, S., et al., "Improved estimation of aerosol optical depth from MODIS imagery over land surfaces", Remote Sensing of Environment, vol 104, no. 4, pp.416-425, 2006, doi: 10.1016/j.rse.2006.05.016.
[52].Wang, X., et al., "Influences of forest on MODIS snow cover mapping and snow variations in the Amur River basin in Northeast Asia during 2000–2014", Hydrological Processes, vol 31, no. 18, pp.3225-3241, 2017, doi: 10.1002/hyp.11249.
[53].Vikhamar, D. and R. Solberg (2003). "Subpixel mapping of snow cover in forests by optical remote sensing." Remote Sensing of Environment 84: 69-82.
[54].Mazzotti, G., et al., "Revisiting Snow Cover Variability and Canopy Structure Within Forest Stands: Insights From Airborne Lidar Data", *Water Resources Research*, vol 55, no. 7, pp.6198-6216, 2019, doi: 10.1029/2019wr024898.
[55].Rittger, K., et al., "Canopy Adjustment and Improved Cloud Detection for Remotely Sensed Snow Cover Mapping", *Water Resources Research*, vol 56, no. 6, 2020, doi: 10.1029/2019wr024914.

Jinyu Huang (Member, IEEE) received the B.S. degree from Nanjing normal university, Nanjing, China, in 2021. He is currently working toward the Ph.D. in cartography and geography information system at Beijing Normal University, Beijing. He researches interests include remote sensing of snow, in particular mapping snow-covered areas with Chinese satellites.

Lingmei Jiang (Member, IEEE) received the Ph.D. degree in geography from Beijing Normal University, Beijing, China, in July 2005. She is a Professor with the Faculty of Geographical Science, Beijing Normal University. She has authored/coauthored over 200 scientific publications. Her research interests include microwave emission/scattering modeling of the land surface, passive microwave remote sensing of snow water equivalent and soil moisture, surface freeze/thaw state, and remote sensing data assimilated into the land surface model. Dr. Jiang has been received with the Shi Yafeng Award for Young Scientists in Cryosphere and Environment in 2018, and Li Xiaowen Remote Sensing Science Award in 2023.

Fangbo Pan received the B.S. degree from Zhengzhou University, Zhengzhou, China, in 2016, the M.S. degree from University of Chinese Academy of Sciences, Beijiing, China, in 2019. He is currently working toward the Ph.D. in cartography and geography information system at Beijing Normal University, Beijing. He researches interests include remote sensing of snow, in particular mapping snow-covered areas with geostationary meteorological satellites.

Bo Zhong received the B.S. degree in geology from the Department of Earth Science, Zhejiang University, Hangzhou, China, in 2001, the M.S. degree in cartography and GIS from the Institute of Remote Sensing Applications, Chinese Academy of Science, Beijing, China, in 2004, and the M.A. degree in geography from the University of Maryland, College Park, MD, USA, in 2006.

He is currently an Associate Professor in Aerospace Information Research Institute, Chinese Academy of Sciences, Beijing, China. His research interests include land-use and land cover change, remote sensing image processing, and remote sensing of aerosol.

Shengli Wu received the B.S. degree in environmen- tal science from Peking University, Beijing, China, in 2001, and the Ph.D. degree in cartography and geography information system from the Institute of Remote Sensing Application, Chinese Academy of Sciences, Beijing, in 2006.

He is currently a Research Scientist with the National Satellite Meteorological Center, China Meteorological Administration, Beijing. He is a Principal Investigator of the Microwave Radiation Imager instrument onboard FengYun-3C, 3D, 3F,and 3G platform, leading the ground cal/val and data preprocessing work. His research interests include microwave radiometer calibration and snow and ice parameters retrieval.

Dr. Wu acts as the Co-Chair of the Microwave Subgroup of Global Space- Based Inter-Calibration System (GSICS, a W.M.O.-sponsored international cooperation).

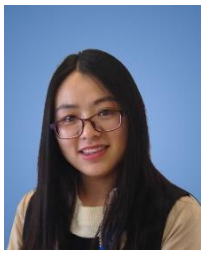

Huizhen Cui is currently a research assistant at National Space Science Center, Chinese Academy of Sciences. She received the Ph.D. degree in cartography and geographic information system at Faculty of Geographical Science, Beijing Normal University, China, in July, 2019. From 2017 to 2018, she was a Visiting Ph.D. Student with the Institute of Applied Physics, National Research Council (IFAC-CNR), Florence, Italy.

Her research interests include the microwave remote sensing of soil moisture and microwave emission and scattering modelling of land surface.